Meteorological Influence on L-Band Forest Backscatter: Evidence from the BorealScat-2 Radar Tower

Shivam Rawat[1,*], Albert R. Monteith[2], Lars M.H. Ulander[2], Hjalmar Laudon[3], Jose Gutierrez Lopez[3], Henrik J. Persson[1]

[1] Department of Forest Resource Management, Swedish University of Agricultural Sciences, Umeå, Sweden
[2] Department of Space, Earth and Environment, Chalmers University of Technology, Gothenburg, Sweden
[3] Department of Forest Ecology and Management, Swedish University of Agricultural Sciences, Umeå, Sweden

Keywords: Boreal forests, L-band radar, backscatter time series, Forest water dynamics, Vapour pressure deficit (VPD), Meteorological forcing.

Abstract

Boreal forest water exchange operates at sub-daily time scales, yet these dynamics are difficult to resolve using conventional satellite radar observations. In this study, height-resolved L-band measurements from the BorealScat-2 radar tower at Svartberget, northern Sweden, were analysed together with co-located Integrated Carbon Observation System (ICOS) meteorological observations to investigate how external atmospheric forcing affects forest radar backscatter during the meteorological summer of 2024. Two related questions were addressed: (1) whether dry-day diurnal radar variability is more closely linked to incoming shortwave radiation or atmospheric demand, and (2) how rainfall responses vary with polarization and forest layer. Under dry-demand conditions, incoming shortwave radiation (SW_IN) peaked before vapour pressure deficit (VPD), while the radar response peaked later. The strongest dry-day amplitude was observed in horizontally co-polarized (HH) ground backscatter, whereas vertically co-polarized (VV) canopy backscatter responded later and with smaller amplitude. Profile-based metrics further indicated an afternoon downward redistribution of the effective scattering centre. During rainfall, the strongest positive wetting responses occurred in canopy and upper-canopy levels, especially in VV, while HH ground backscatter showed an opposite-sign response. Multi-pulse rainfall events produced substantially larger anomalies than single-pulse events. These results support two contrasting short-term response regimes in boreal L-band backscatter: a dry-demand redistribution regime and a rain-driven wetting/interception regime.

1. Introduction

Understanding how external meteorological parameters impact the forest water exchange mechanism remains a key challenge in radar ecohydrology. Sub-daily variations in atmospheric demand and rainfall in boreal forests can alter attenuation, scattering-path redistribution, and canopy wetness, although these processes cannot be easily resolved with traditional satellite SAR due to a gap between the revisit time and the natural daily cycle. Tower-based radar experiments therefore offer a unique opportunity to observe how short-term meteorological forcing, such as incoming radiation, atmospheric demand, temperature, wind, and rainfall, is reflected in the radar signal.

The BorealScat-2 system is a multi-polarization, multi-frequency tomographic radar installed on a 50 m tower in northern Sweden and has already demonstrated to capture diurnal variations in boreal forest backscatter, with phase and amplitude differences across bands and polarizations (Monteith et al., 2024). Earlier BorealScat analyses further demonstrated that densely sampled tomographic radar observations can separate backscatter from different forest heights and resolve temporal effects of diurnal forcing, wind, and rainfall in boreal forest conditions (Monteith and Ulander, 2021).

The repeatability of such tower-based tomographic imaging in natural media relies on robust system calibration, as demonstrated by Monteith et al. (2019). How dry-day diurnal L-band variability can be explained in terms of incoming radiation, vapour pressure deficit (VPD), temperature, and wind is an interesting question. This question is particularly important because a recent study showed that canopy-only backscatter can decrease as stem water content increases, if the associated increase in canopy attenuation outweighs the increase in canopy scattering (Leistner et al., 2026). In other words, the common assumption that more vegetation water always yields higher backscatter is too simple for boreal L-band tomography. Instead, external atmospheric forcing may alter the radar signal through changes in attenuation, redistribution of scattering contributions, and shifts in the effective scattering height.

A second open question concerns rain-driven wetting/interception responses and how they vary with polarization, canopy layer, and rainfall event structure. Earlier work showed that radar backscatter is sensitive to rainfall interception and canopy water storage, and that the sign and magnitude of the response can depend strongly on forest structure and canopy closure (de Jong et al., 2000). Tower-radar experiments in forest environments, such as TropiSCAT, also highlighted the importance of canopy wetness and structure for radar backscatter dynamics (Albinet et al., 2012). These findings show that rainfall response should not be treated as a simple wet/dry contrast: the signal will depend on which canopy layer is observed, which polarization is used, and the amount of rainfall over time.

An additional complexity arises from polarization, since co-polarized and cross-polarized channels can behave differently (Cloude and Pottier, 1996). Together with height-resolved tomography, this creates an opportunity for various L-band channels to evaluate the impact of external parameters on forest water dynamics. In this study, we use height-resolved BorealScat-2 L-band observations together with closely co-located ICOS meteorological measurements to investigate two related objectives:

(1) dry-demand redistribution, characterized by diurnal variability and vertical shifts under rain-free daytime forcing;

https://doi.org/10.5194/isprs-archives-XLIX-B1-2026-209-2026 | © Author(s) 2026. CC BY 4.0 License.

(2) polarization- and height-dependent sensitivity to external forcing, including both dry atmospheric demand and rain-driven wetting/interception responses.

More broadly, the study helps connect sub-daily tower observations to the interpretation of future spaceborne SAR observations, since tower-based and satellite backscatter have already been shown to agree well enough for tower data to reveal limitations and new mission needs in forest monitoring (Leistner et al., 2023).

2. Materials and Methods

2.1 Study area

The study area is located at Svartberget Research Station in northern Sweden (64.24° N, 19.77° E), 60 km northwest of Umeå. It is a boreal forest dominated by Norway spruce (*Picea abies*) and Scots pine (*Pinus sylvestris*), with average canopy heights of about 25–27 m.

The region's climate is boreal, with very long, cold winters and relatively short summers. Precipitation is about 600-700 mm per annum, and seasonal water movement is highly regulated by temperature, radiation, and atmospheric demand during the growing season.

This study focused on the meteorological summer (MetSummer) of 2024, as defined by the Swedish Meteorological and Hydrological Institute (SMHI). Under this definition, summer begins when the daily mean air temperature exceeds 10 °C for five consecutive days, resulting in a summer period extending from 12 May to 25 September 2024.

2.2 BorealScat-2 Radar Data

Radar observations were obtained using the BorealScat-2 radar tower located at the Svartberget Research Station, as shown in Figure 1. It is equipped with a moving array of antennas that monitor changes in the forest at 30-minute intervals, providing much denser temporal observations than satellite-based systems. Because of high temporal resolution, the radar tower enables examination of how forest backscatter changes over a single day as environmental conditions evolve.

The radar tower operates at several frequencies, including P (435 MHz), ultra-high frequency (UHF, 600 MHz), L (1270 MHz), and C (5400 MHz) bands. This study focuses on L-band radar observations because they can penetrate the forest canopy and interact with multiple components of the forest, including branches, stems, and the ground. The tower has 20 vertically oriented antennas at its top. The antennas are connected to a 20-port vector network analyzer, with one port per antenna. With such a setup, it is possible to conduct fast, coherent measurements. The decorrelation of the wind is often negligible because a tomographic measurement is much shorter than the time over which wind-induced decorrelation occurs. The time-domain back-projection technique is then used to reconstruct the tomographic images (Monteith et al., 2024).

Each radar frequency has 4 polarization channels: HH, VV, HV, and VH, where measurements are made with 30-minute intervals. Co-polarized channels (HH and VV) tend to be influenced more strongly by structural elements such as stems, whereas cross-polarized channels (HV and VH) often capture volume scattering from canopy elements. To better interpret where scattering originates, radar backscatter was averaged across several representative vertical layers, including the ground layer, canopy layer, upper canopy, and the full forest layer.

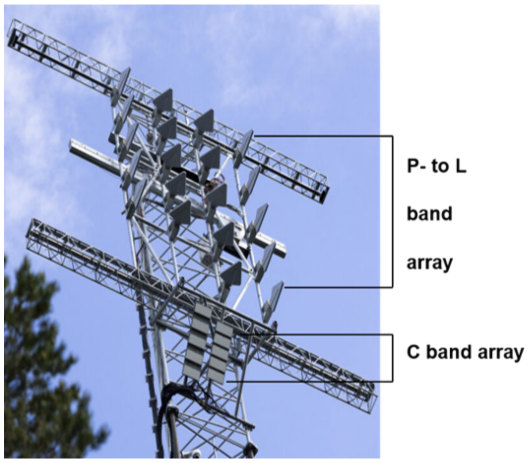

Figure 1. BorealScat-2 Radar Tower with a moving array of antennas located at Svartberget Research Station in northern Sweden.

2.3 ICOS Meteorological Data

Meteorological measurements used in this study were obtained from the ICOS mast located close to the radar tower. The 150 m mast provides a dense time series of different meteorological variables and atmospheric fluxes that govern water exchange processes in the boreal forest (Peichl et al., 2025).

For this study, we selected the most important meteorological variables to represent the main external drivers of forest water exchange. These include air temperature (TA), vapour pressure deficit (VPD), incoming shortwave radiation (SW_IN), precipitation (P), and wind speed (WS). These variables influence evapotranspiration, canopy wetness, and atmospheric demand, which in turn affect the dielectric properties and scattering behaviour of vegetation/forest observed by radar.

These ICOS observations, therefore, provide essential environmental context for interpreting the radar signals and investigating how meteorological factors modulate forest water dynamics.

3. Methodology

3.1 Data Processing

The meteorological measurements were aligned with the BorealScat-2 radar timestamps at 30-minute intervals, enabling direct comparison between sub-daily radar backscatter variations and atmospheric forcing conditions. Synchronizing the datasets enabled direct comparison of radar backscatter with atmospheric conditions throughout the study period. Radar and meteorological data were aligned on a common UTC timeline during preprocessing. For diurnal analyses, including daily harmonics, dry-day composites, and reported timing metrics, timestamps were converted to local time (Europe/Stockholm).

Basic quality control was applied to remove clearly invalid or missing measurements. Figure 2 shows the time-series data used in the analyses for MetSummer.

Using a temperature-based seasonal definition helps ensure the analysis captures the period when boreal forests are most active in water exchange. Once the datasets were synchronized and the seasonal window defined, the combined radar and meteorological time series were used for the analyses described in the following section.

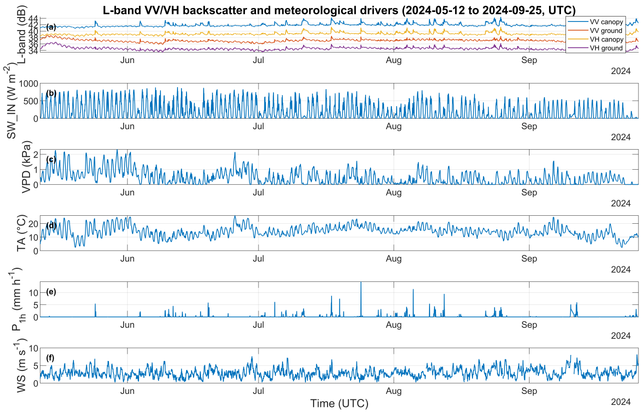

Figure 2. Time series of L-band radar backscatter and meteorological variables from 12 May 2024 to 25 September 2024 (UTC). Panel (a) shows L-band VV and VH backscatter for the canopy and ground layers, expressed in dB. Panels (b)–(f) show the corresponding meteorological drivers, namely air temperature (TA, °C), vapour pressure deficit (VPD, kPa), incoming shortwave radiation (SW_IN, W m^{-2}), one-hour running precipitation rate (P, mm h^{-1}), and wind speed (WS, m s^{-1}). Note that the backscatter values are only approximately calibrated, i.e., they have a constant but unknown offset.

3.2 Data Preparation and Radar Metrics

The analysis uses L-band radar observations acquired at a 30 min sampling interval. For each acquisition time t, the forest profile was divided into four height layers representing ground (-5 to 3 m), canopy (3 to 26 m), upper canopy (14 to 22 m), and full forest (-5 to 26 m). These layers are denoted as $\mathcal{L}_{\text{ground}}$, $\mathcal{L}_{\text{canopy}}$, $\mathcal{L}_{\text{upper\_canopy}}$, and $\mathcal{L}_{\text{forest}}$, respectively, and are defined as:

$$\mathcal{L}_{\text{ground}} = [-5,\, 3]\ \text{m}, \qquad \mathcal{L}_{\text{canopy}} = [3,\, 26]\ \text{m},$$

$$\mathcal{L}_{\text{upper\_canopy}} = [14,\, 22]\ \text{m}, \qquad \mathcal{L}_{\text{forest}} = [-5,\, 26]\ \text{m}.$$

These layer definitions allow the vertical distribution of radar backscatter to be analysed in a physically interpretable way across different parts of the forest profile.

For each polarization $p \in \{HH, VV, HV, VH\}$, let $B_p(z_i, t)$ denote the radar backscatter profile in dB at height bin z_i and time t. The mean backscatter for layer $\mathcal{L}$ was computed as given in Eq. (1).

$$B_{p,\mathcal{L}}(t) = \frac{1}{N_{\mathcal{L}}} \sum_{z_i \in \mathcal{L}} B_p(z_i, t), \tag{1}$$

where $N_{\mathcal{L}}$ is the number of vertical bins within layer $\mathcal{L}$.

Additional profile-based metrics were also derived. The median scattering height $h50(t)$ was defined as the height satisfying

$$\sum_{z_i \le h50(t)} P(z_i, t) \ \ge\ 0.5 \sum_{z_i} P(z_i, t),$$

where $P(z_i, t)$ denotes the radar power profile at height bin z_i and time t.

An additional profile-based metric was defined as the ground scattering fraction $F_{\text{ground}}(t)$, representing the fraction of total radar power originating from near-ground heights:

$$F_{\text{ground}}(t) = \frac{\sum_{z_i \in \mathcal{L}_{\text{ground}}} P(z_i, t)}{\sum_{z_i \in \mathcal{L}_{\text{forest}}} P(z_i, t)} \tag{2}$$

where $P(z_i, t)$ denotes the radar power profile at height bin z_i and time t, and the summations are taken over the ground layer $\mathcal{L}_{\text{ground}}$ and the full forest profile $\mathcal{L}_{\text{forest}}$, respectively.

A simple canopy contrast metric was also computed as the canopy cross-polarization ratio

$$\text{CPR}(t) = \overline{B}_{HV,\text{canopy}}(t) - \overline{B}_{HH,\text{canopy}}(t),$$

expressed in dB.

Meteorological variables were extracted from the radar-interpolated time series and included incoming shortwave radiation $\text{SW\_IN}(t)$, vapour pressure deficit $\text{VPD}(t)$, air temperature $\text{TA}(t)$, wind speed $\text{WS}(t)$, and precipitation $P(t)$.

Rainfall values below a prescribed threshold $P_{\min}$ were set to zero:

$$P^*(t) = \begin{cases} 0, & P(t) < P_{\min}, \\ P(t), & P(t) \ge P_{\min}. \end{cases}$$

Rolling precipitation totals were computed over the preceding 6 h and 24 h windows as defined in Eq. (3).

$$P_{6\text{h}}(t) = \sum_{\tau = t - 6\text{h}}^{t} P^*(\tau), \qquad P_{24\text{h}}(t) = \sum_{\tau = t - 24\text{h}}^{t} P^*(\tau), \tag{3}$$

where $P^*(t)$ is the thresholded precipitation at time t, τ indexes the discrete time steps (at 30 min resolution), and each summation includes all samples within the corresponding backward-looking time window.

3.3 Dry-day selection and daily harmonic characterization

Because the objectives concern externally forced diurnal behaviour, the analysis was restricted to days with sufficiently dry daytime conditions. A dry-demand mask $D(t)$ was defined to identify time steps dominated by daytime atmospheric forcing. The mask was defined such that

$$D(t) = 1 \text{ if}$$

$$\text{SW\_IN}(t) > 150\ \text{W m}^{-2},$$

$$\text{VPD}(t) > 0.3\ \text{kPa},$$

$$P_{6\text{h}}(t) < 0.1\ \text{mm},$$

and

$$D(t) = 0 \text{ otherwise.}$$

To prevent residual wetting effects, a day d was retained only if all of the following conditions were satisfied:

$$P_{24h}(d) < 1\ \text{mm},$$

$$N_{\mathrm{dry}}(d) \geq 10,$$
$$f_{\mathrm{dry}}(d) \geq 0.90,$$
$$P_{\mathrm{day}}(d) < 0.20\,\mathrm{mm},$$

where $N_{\mathrm{dry}}(d)$ is the number of valid dry-demand samples during the day, $f_{\mathrm{dry}}(d)$ is the fraction of dry samples during the demand period, and $P_{\mathrm{day}}(d)$ is the total daily rainfall.

For each retained day, a 24 h harmonic model was fitted separately to radar metrics and meteorological variables, as given in Eq. (4). The daily harmonic amplitude A was then computed from the fitted coefficients using Eq. (5), and the corresponding peak timing t_{peak} was derived using Eq. (6). These quantities were used to summarize the strength and timing of the diurnal cycle.

$$y(t) = a_0 + a_1 \cos\left(\frac{2\pi t}{24}\right) + b_1 \sin\left(\frac{2\pi t}{24}\right) + \varepsilon(t), \quad (4)$$

where a_0 is the mean level, a_1 and b_1 are harmonic coefficients, and $\varepsilon(t)$ is the residual term. The daily harmonic amplitude A was computed as

$$A = \sqrt{a_1^2 + b_1^2}, \quad (5)$$

and the phase timing was obtained from the fitted coefficients using the two-argument arctangent function. The corresponding peak timing t_{peak} (in hours) was derived as

$$t_{\mathrm{peak}} = \mathrm{mod}\left(\frac{1}{\omega}\,\mathrm{atan2}(b_1, a_1),\, 24\right), \qquad \omega = \frac{2\pi}{24}. \quad (6)$$

Daily fits were filtered using minimum goodness-of-fit thresholds of $R^2 \geq 0.50$ for meteorological variables and $R^2 \geq 0.30$ for radar metrics. In addition, half-hour composites of the retained dry days were used to extract timing markers, including the peak of SW_IN, the peak of VPD, the minimum of $h50$, and the maximum of the ground scattering fraction.

3.4 Meteorological attribution of dry-day diurnal radar cycles

Objective 1 focused on dry-demand conditions during MetSummer. Here, we quantified how dry-day diurnal radar variability was related to external meteorological forcing. This analysis was restricted to the dry-demand mask described above.

To isolate the diurnal signal, low-frequency background variability was removed using a moving-median high-pass filter, as defined in Eq. (7).

$$x'(t) = x(t) - \mathrm{median}_{\tau \in [t-1.5\,\mathrm{d},\, t+1.5\,\mathrm{d}]}\{x(\tau)\} \quad (7)$$

where $x(t)$ denotes the radar time series (e.g., backscatter or derived metric), $x(\tau)$ denotes the same time series evaluated at time τ within the moving window, and the median is computed over a 3-day window centred at time t.

To attribute radar variability to meteorological forcing, moving-window regressions were applied using 5-day windows advanced by 1 day. Let $y(t)$ denote the radar metric and $\mathbf{X}(t)$ the set of meteorological predictors. A linear model was fitted as given in Eq. (8).

$$\begin{aligned} y(t) = \beta_0 + \beta_1\,\mathrm{SW\_IN}(t) + \beta_2\,\mathrm{VPD}(t) \\ + \beta_3\,\mathrm{TA}(t) + \beta_4\,\mathrm{WS}(t) + \epsilon(t) \end{aligned} \quad (8)$$

where $y(t)$ is the radar metric at time t, β_0 is the intercept, β_1–β_4 are regression coefficients associated with incoming shortwave radiation, vapour pressure deficit, air temperature, and wind speed, respectively, and $\epsilon(t)$ is the residual term.

Attribution was performed using a sequential, order-dependent residualized decomposition. Predictors were entered in the order:

$$\mathrm{SW\_IN} \rightarrow \mathrm{VPD} \rightarrow \mathrm{TA} \rightarrow \mathrm{WS}$$

Shortwave radiation was treated as the primary external driver of the daytime cycle, while VPD, air temperature, and wind speed were added to quantify additional variance beyond this base forcing. The predictor order was physically motivated by the common hierarchy of environmental controls on transpiration and stomatal/canopy conductance, with radiation as the primary energy driver, VPD as the main atmospheric demand term, temperature as a secondary thermodynamic control, and wind as a modulating perturbation.

The incremental contribution of each predictor was quantified using the change in explained variance as described in Eq. (9).

$$\Delta R_k^2 = R^2_{\text{with } k} - R^2_{\text{without } k} \quad (9)$$

where R_k^2 is the model including predictor k and R_{k-1}^2 is the model without it. Accordingly, ΔR_k^2 represents the additional variance explained by predictor k, conditional on all previously included predictors. The resulting contributions should therefore be interpreted as incremental and order-dependent rather than as unique causal effects.

Bootstrap resampling by day was used to estimate confidence intervals for the key summary statistics, ensuring robustness against day-to-day variability.

3.5 Polarization sensitivity to atmospheric demand and rainfall events

Objective 2 focused on how the radar response depended on polarization and height layer under two contrasting external forcing conditions: (i) dry atmospheric demand, and (ii) rain-driven wetting/interception events.

For the dry-demand component of Objective 2, daily radar harmonic amplitudes were correlated with daily VPD harmonic amplitudes for each polarization–layer channel using Spearman's rank correlation. Let $A^{(d)}_{\mathrm{radar}}$ and $A^{(d)}_{\mathrm{VPD}}$ denote the daily amplitudes for day d. The correlation coefficient was computed using Eq. (10).

$$\rho = \mathrm{corr}_{\mathrm{Spearman}}\left(A^{(d)}_{\mathrm{radar}}, A^{(d)}_{\mathrm{VPD}}\right) \quad (10)$$

This non-parametric measure captures monotonic relationships between radar variability and atmospheric demand without assuming linearity.

For the rainfall component, events were detected after a 6 h dry gap and required at least 6 h separation between event starts. Event end was defined after at least 2 h without rain, with a maximum look-ahead of 24 h. Let $P(t)$ denote the precipitation time series. For each event starting at time t_0, cumulative rainfall metrics were computed over the preceding time windows as defined in Eq. (11).

$$P_{\mathrm{sum},\Delta t}(t_0) = \int_{t_0-\Delta t}^{t_0} P(t)\,dt \tag{11}$$

where $\Delta t \in \{1\,\mathrm{h},\,3\,\mathrm{h},\,6\,\mathrm{h}\}$. The total rainfall associated with each event was computed as given in Eq. (12).

$$P_{\mathrm{total}} = \int_{t_{\mathrm{start}}}^{t_{\mathrm{end}}} P(t)\,dt \tag{12}$$

Events were then classified as multi-pulse if they satisfied the duration or rainfall-structure criteria defined in Eq. (13).

$$\frac{P_{\mathrm{sum,6h}}}{P_{\mathrm{sum,1h}}} \geq 1.5 \quad \text{and} \quad P_{\mathrm{sum,6h}} - P_{\mathrm{sum,1h}} \geq 0.3\,\mathrm{mm} \tag{13}$$

Otherwise, they were classified as single-pulse events.

Radar rain responses were analysed on diurnal-anomaly series rather than raw backscatter. A half-hour climatology was first constructed from the retained dry days for each radar channel, and anomaly series were then obtained by subtracting the climatological mean at the corresponding local half-hour bin from the observed radar backscatter.

For each real rainfall event, a matched set of control windows was selected within ± 60 days, constrained to the same local half-hour bin and dry conditions. Let $\tilde{x}_{\mathrm{real}}$ and $\tilde{x}_{\mathrm{control}}$ denote the median anomaly over real and control windows, respectively. The rain-induced signal is quantified in Eq. (14):

$$\Delta x = \tilde{x}_{\mathrm{real}} - \tilde{x}_{\mathrm{control}} \tag{14}$$

Additional summaries were produced for a low-wind subset (WS $\leq 4\ \mathrm{m\,s^{-1}}$), and separately for single- and multi-pulse events. This framework allows rain-driven radar responses, quantified by Eq. (14), to be isolated from the underlying diurnal cycle while accounting for variability due to seasonal and atmospheric conditions.

4. Results and Discussion

Results are presented in two complementary parts. Section 4.1 examines dry-demand diurnal dynamics under rain-free daytime conditions and evaluates their meteorological attribution, with emphasis on phase behaviour, amplitude variability, and vertical redistribution of effective scattering. Section 4.2 examines polarization- and height-dependent sensitivity to external forcing, first through demand-related channel behaviour under dry conditions and then through rain-event responses characterized by wetting/interception effects and differences between single- and multi-pulse rainfall events.

4.1 Dry-demand diurnal dynamics

Objective 1 examined whether diurnal radar variability follows radiation or atmospheric demand more closely, and whether the height-resolved signal shows a coherent redistribution through the day. The dry-demand signal was small in absolute magnitude but highly consistent. The strongest harmonic amplitude occurred in the HH ground (~0.22 dB), whereas the VV canopy was smaller (~0.11 dB). As shown in Table 1, the main Objective 1 dry-condition metrics summarize the phase timing, harmonic amplitude, and incremental explained variance (ΔR^2) for the key variables and radar channels.

The forcing sequence was also physically coherent: SW_IN peaked first at ~13.0 h, followed by VPD at ~14.0 h, while the radar response occurred later in the afternoon. HH ground backscatter peaked at ~15.0 h, closest to the VPD maximum, whereas VV canopy backscatter peaked later at ~16.0 h. Under these conditions, radar backscatter does not simply increase or decrease; instead, it shows a downward shift in effective scattering height, with the peak closer to VPD maximum than to the incoming radiation, indicating a redistribution of scattering contributions driven by atmospheric demand. At the same time, the tomographic metrics showed a clear afternoon downward redistribution of the effective scattering profile: VV $h50$ reached its minimum at ~14.5 local time, while VV F_{ground} peaked at ~14.0 local time. The canopy cross-polarization ratio (CPR = HV − HH) (Figure 3) also showed a less distinct diurnal pattern, with lower values in the late morning and higher values later in the day, indicating that the dry-day cycle affected not only radar intensity and scattering height but also the relative polarization response of the canopy. Figure 3 shows coordinated dry-day changes in radar intensity, polarization behavior, and scattering-height distribution under external forcing.

This pattern is consistent with increasing atmospheric drying demand during the day. In radar terms, it points to an interplay between attenuation and backscatter, with the balance between canopy and sub-canopy contributions changing throughout the day. Earlier BorealScat work linked scattering-height metrics to tree-water indicators such as stem radius, providing precedent for interpreting these height-resolved radar signals (Monteith et al., 2024). More recent BorealScat-2 modelling work also showed that, at L-band, canopy-only backscatter can even decrease with increasing stem water content when the associated increase in canopy attenuation outweighs the increase in canopy scattering (Leistner et al., 2026). In other words, the old assumption that “more water always means more backscatter” is too simple for boreal L-band tomography.

Table 1. Main Objective 1 results for MetSummer, summarizing dry-day diurnal timing, height redistribution, and meteorological attribution of L-band radar variability.

Variable / metric	Value	Unit
SW_IN peak	13.0	h (local time)
VPD peak	14.0	h (local time)
HH ground peak	15.0	h (local time)
VV canopy peak	16.0	h (local time)
VV $h50$ minimum	14.5	h (local time)
VV F_{ground} peak	14.0	h (local time)
HH ground amplitude	0.22	dB
VV canopy amplitude	0.11	dB
HH ground ΔR^2 from VPD	0.26	unitless
VV canopy ΔR^2 from VPD	0.17	unitless

Note: ΔR^2 is the order-dependent incremental increase in explained variance obtained when a predictor is added to the sequential residualized decomposition.

The attribution analysis supported this interpretation because VPD explained additional radar variance even after accounting for the part shared with SW_IN, indicating that dry-day radar variability was linked to atmospheric demand rather than to radiation alone. The median increase in explained variance

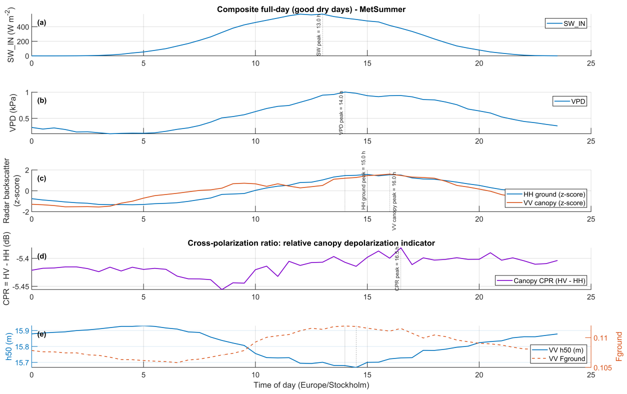

Figure 3. Composite half-hourly dry-day cycles for MetSummer based on good dry days. Panels show (a) SW_IN (W m^{-2}), (b) VPD (kPa), (c) z-scored HH ground and VV canopy backscatter, (d) canopy CPR = HV − HH (dB), and (e) VV $h50$ with VV ground scattering fraction (F_{ground}). Vertical dashed lines mark key timing points such as the SW_IN peak, VPD peak, HH ground peak, VV canopy peak, CPR peak, $h50$ minimum, and F_{ground} peak. Note: All timing values are reported in local time. (Europe/Stockholm).

was about 0.26 for HH ground and 0.17 for VV canopy, while adding wind improved the full model but did not remove the VPD effect. This indicates that the dry-demand signal is not solely due to canopy motion. Overall, Objective 1 shows that under dry conditions, L-band diurnal variability is more closely aligned with atmospheric demand than with radiation alone, and that this is accompanied by a height-resolved redistribution of the effective scattering contribution.

The variance decomposition indicates that dry-day L-band backscatter in MetSummer is driven by a combination of SW_IN, VPD, temperature, and wind, but their relative importance varies strongly across channels. HH canopy shows a notable split between VPD and wind, but Figure 4 indicates that this broader pattern of shared VPD and wind influence is also present in other channels. Figure 4 shows that the relative importance of external drivers depends strongly on polarization and height layer, with substantial wind contributions in several canopy and upper-canopy layers, while some ground layers are more strongly associated with the SW_IN base term.

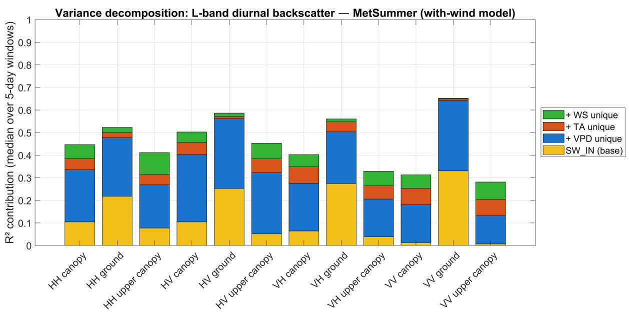

Figure 4. Sequential variance decomposition of dry-day L-band diurnal backscatter for MetSummer under the with-wind model. Each stacked bar represents one polarization–layer channel, and the total bar height gives the median explained variance (R^2) over 5-day windows. The coloured segments show the ordered contributions of SW_IN (base), plus the additional variance explained by VPD, air temperature (TA), and wind speed (WS).

4.2 Rainfall-event-response wetting and interception response

Before analyzing rainfall-event responses, we first examined whether the day-to-day strength of the dry-demand radar cycle depended on atmospheric demand itself. To do this, we correlated daily radar harmonic amplitude with daily VPD harmonic amplitude for each polarization–layer channel. The resulting pattern (Figure 5) shows that demand sensitivity was positive in most channels, but its strength varied by polarization and height layer. The strongest coupling occurred in HH, with correlations of $\rho = 0.52$ in the ground layer, $\rho = 0.52$ in the canopy layer, $\rho = 0.51$ in the upper canopy, and $\rho = 0.58$ in the full forest. HV also showed moderate positive correlations across all layers ($\rho = 0.36$ to 0.46). By contrast, VV and VH exhibited weaker but still generally positive associations, with VV ranging from $\rho = 0.10$ to 0.40 and VH from $\rho = 0.22$ to 0.32. Overall, these results indicate that short-term demand sensitivity is polarization-dependent, with the clearest coupling in HH and more moderate but still detectable responses in HV, VV, and VH across the forest profile.

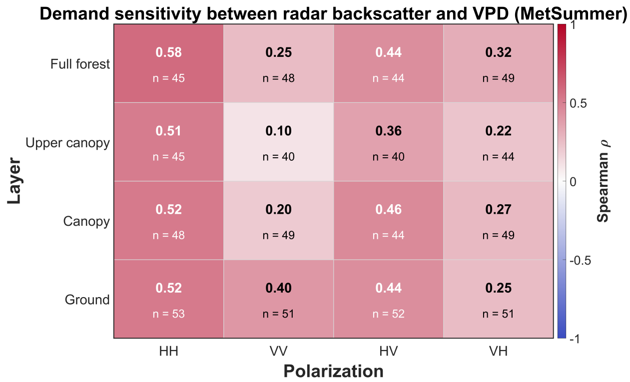

Figure 5. Demand sensitivity of L-band radar diurnal amplitude to atmospheric demand during MetSummer. Heatmap of Spearman’s rank correlation coefficient (ρ) between daily radar harmonic amplitude (A_{radar}) and daily vapour pressure deficit harmonic amplitude (A_{VPD}) for each polarization–layer channel. Values in each cell give the correlation coefficient and the number of retained dry days.

Having identified which channels show the clearest coupling to atmospheric demand under dry conditions, we next examined how the same polarization-layer channels responded to rainfall events for MetSummer.

The comparison between rain-event types (Figure 6) showed that multi-pulse events produced substantially larger radar responses than single-pulse events across most polarization–layer channels. In the canopy layer, multi-pulse responses reached +0.82 dB (VV), +0.66 dB (HH), +0.64 dB (HV), and +0.60 dB (VH), compared to single-pulse values of +0.22, +0.19, +0.21, and +0.15 dB, respectively. A similar pattern was observed in the upper canopy, where multi-pulse responses were +0.82 dB (VV), +0.69 dB (HH), +0.64 dB (HV), and +0.56 dB (VH), while single-pulse responses ranged from +0.18 to +0.21 dB.

In the full-forest layer, multi-pulse events also showed strong responses, reaching +0.81 dB (VV), +0.67 dB (HH), +0.61 dB (HV), and +0.66 dB (VH), compared to single-pulse values between +0.22 and +0.26 dB. By contrast, the ground layer exhibited weaker and more variable behaviour. While multi-pulse events produced positive responses in VV (+0.14 dB), HV (+0.13 dB), and VH (+0.22 dB), HH remained negative and became more negative for multi-pulse events (−0.31 dB) compared to single-pulse events (−0.18 dB). Overall, these results show that multi-pulse rainfall events consistently amplify canopy and upper-canopy wetting/interception signals across all polarizations, whereas ground-layer responses are weaker, more mixed, and polarization-dependent.

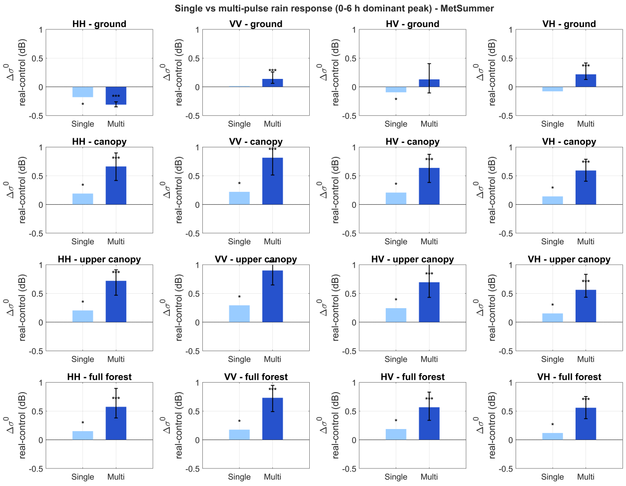

Figure 6. Single- versus multi-pulse rain responses for the dominant 0–6 h real-minus-control L-band anomaly in MetSummer. Multi-pulse rainfall events produced substantially larger radar responses than single-pulse rainfall events in most canopy, upper-canopy, and full-forest channels, whereas single-pulse effects were generally weak or negligible. Note, the weaker response of single-pulse events should be interpreted cautiously, as very short precipitation pulses may partly reflect the discretized nature of the gauge record rather than sustained canopy wetting.

To summarize the polarization-group behaviour in Objective 2, we compared co-polarized (HH, VV) and cross-polarized (HV, VH) responses across the main dry-demand and rainfall metrics. In general, co-pol channels showed stronger coupling to atmospheric demand and stronger rainfall-event responses than cross-pol channels, while the largest wetting-related contrasts occurred in canopy and upper-canopy layers. Multi-pulse events also produced consistently larger responses than single-pulse events, especially in the upper canopy, reinforcing the interpretation that sustained rainfall primarily amplifies canopy-associated wetting and interception effects. Figure 7 highlights stronger wetting-related contrasts in canopy and upper-canopy layers and generally stronger co-pol than cross-pol responses, while also showing that sustained rainfall produces larger radar anomalies than single-pulse events.

5. Conclusion

This study showed that height-resolved L-band BorealScat-2 observations capture two main radar states in a boreal forest under changing external forcing.

Under dry daytime conditions, the dominant signal was a demand-driven redistribution of scattering through the forest profile, with vapour pressure deficit explaining additional variability beyond incoming shortwave radiation, while wind also played an important role in several canopy and upper-canopy channels. During and after rain events, the dominant signal

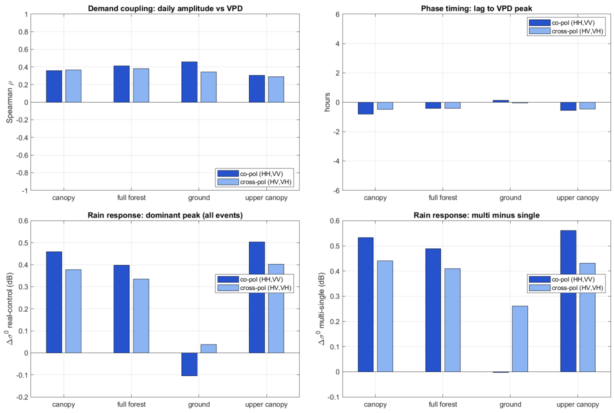

Figure 7. Synthesis of co-polarized and cross-polarized behaviour during MetSummer. Co-polarized channels (HH, VV) and cross-polarized channels (HV, VH) are summarized by the forest layer for four diagnostics: demand coupling between daily radar amplitude and daily VPD amplitude, phase timing relative to the VPD peak, rain-event dominant peak response, and the enhancement of multi-pulse relative to single-pulse rainfall responses.

shifted to a wetting/interception response, strongest in the canopy and upper canopy, whereas ground HH showed an opposite-sign response.

The rain-event analysis further showed that this response remained largely significant under low-wind conditions, was much stronger for multi-pulse rain events than for single-pulse rain events, and generally increased with rainfall amount. Together, these results show that short-term L-band radar variability is strongly shaped by external meteorological forcing and depends on both height and polarization.

Overall, the observations support the interpretation that short-term L-band radar variability during summer is governed by two dominant external-forcing regimes: one associated with dry atmospheric demand and vertical redistribution of effective scattering, and another associated with rainfall wetting and interception effects.

These findings are also important for linking tower observations to satellite SAR. A satellite overpass may observe the forest in very different short-term states, such as a dry-demand redistribution state or a rain-driven wetting/interception state, even when the forest structure itself has not changed. Dense tower-based observations therefore help explain part of the temporal variability seen in satellite radar signals and can support a more reliable interpretation of forest SAR observations under changing weather conditions.

Acknowledgment

The authors would like to thank the Bo Rydin Foundation F 12/22, Stiftelsen Seydlitz MP Bolagen 143, Skogssällskapet 2022-1112, Vinnova 2024-00185, FORWARDS Horizon Europe no. 101084481, the Swedish Research Council (VR), the Kempe Foundation, the Knut and Alice Wallenberg Foundation (KAW 2018.0259 and 2023.0245), the Swedish Research Council for Sustainable Development (FORMAS), Kempestiftelserna, and the Swedish Infrastructure for Ecosystem Science (SITES, VR 2017–00635) for funding.

6. References

Albinet, C., Borderies, P., Koleck, T., Rocca, F., Tebaldini, S., Villard, L., Le Toan, T., Hamadi, A., Ho Tong Minh, D., 2012. TropiSCAT: A Ground Based Polarimetric Scatterometer Experiment in Tropical Forests. *IEEE J. Sel. Top. Appl. Earth Obs. Remote Sens.*, 5(3), 1060–1066. doi:10.1109/JSTARS.2012.2201917.

Cloude, S.R., Pottier, E., 1996. A Review of Target Decomposition Theorems in Radar Polarimetry. *IEEE Trans. Geosci. Remote Sens.*, 34(2), 498–518. doi:10.1109/36.485127.

de Jong, J., Klaassen, W., Ballast, A., 2000. Rain Storage in Forests Detected with ERS Tandem Mission SAR. *Remote Sens. Environ.*, 72(2), 170–180. doi:10.1016/S0034-4257(99)00100-5.

Leistner, T., Monteith, A.R., Gutierrez Lopez, J., Ulander, L.M.H., 2026. Estimating Stem Water Content From Tower-Based L-Band Tomographic Radar Using a Single-Scattering Model of a Uniform Layer: A First in situ Experiment. *IEEE J. Sel. Top. Appl. Earth Obs. Remote Sens.*, 19, 3477–3487. doi:10.1109/JSTARS.2025.3650660.

Leistner, T., Monteith, A.R., Ulander, L.M.H., 2023. Comparison of Tower-Based and Satellite L- and C-Band Radar Backscatter From a Boreal Forest. In: *IGARSS 2023 - 2023 IEEE International Geoscience and Remote Sensing Symposium*, 8319–8322. doi:10.1109/IGARSS52108.2023.10283155.

Monteith, A.R., Ulander, L.M.H., Steele-Dunne, S., Bennet, P., Westin, J., Persson, H., Leistner, T., Laudon, H., Fransson, J.E.S., 2024. A Tower-Based Radar Experiment for Studying the Effects of Boreal Forest Tree-Water Relations. *SSRN Electron. J.* doi:10.2139/ssrn.4991471.

Monteith, A.R., Ulander, L.M.H., 2021. Temporal Characteristics of P-Band Tomographic Radar Backscatter of a Boreal Forest. *IEEE J. Sel. Top. Appl. Earth Obs. Remote Sens.*, 14, 1967–1984. doi:10.1109/JSTARS.2021.3050611.

Monteith, A.R., Ulander, L.M.H., Tebaldini, S., 2019. Calibration of a Ground-Based Array Radar for Tomographic Imaging of Natural Media. *Remote Sens.*, 11(24), 2924. doi:10.3390/rs11242924.

Peichl, M., Nilsson, M., Larmanou, E., Smith, P., Marklund, P., De Simon, G., Lofvenius, P., Dignam, R., Holst, J., Molder, M., Andersson, T., Boschetti, F., Kozii, N., Linderson, M., Ottosson-Löfvenius, M., 2025. ETC L2 Meteo from Svartberget, 2018-12-31–2025-09-30. ICOS RI. `https://hdl.handle.net/11676/8oTeFUrMV6_4yC_xeD8PFAkb`.